inorganics

MDPI

Article

Microwave-Mediated Synthesis and Characterization of $Ca(OH)_2$ Nanoparticles Destined for Geraniol Encapsulation

Panagiota Tryfon [1], Nathalie N. Kamou [2], Stefanos Mourdikoudis [3,4,5], George Vourlias [6], Urania Menkissoglu-Spiroudi [2] and Catherine Dendrinou-Samara [1,*]

1 Laboratory of Inorganic Chemistry, Department of Chemistry, Aristotle University of Thessaloniki, 54124 Thessaloniki, Greece
2 Pesticide Science Laboratory, Faculty of Agriculture Forestry and Natural Environment, School of Agriculture, Aristotle University of Thessaloniki, 54124 Thessaloniki, Greece; nnkamou@gmail.com (N.N.K.); rmenkis@agro.auth.gr (U.M.-S.)
3 Biophysics Group, Department of Physics and Astronomy, University College London, London WC1E 6BT, UK; s.mourdikoudis@ucl.ac.uk
4 UCL Healthcare Biomagnetics and Nanomaterials Laboratories, 21 Albemarle Street, London W1S 4BS, UK
5 Separation and Conversion Technology, Flemish Institute for Technological Research (VITO), Boeretang 200, 2400 Mol, Belgium
6 Laboratory of Advanced Materials and Devices, Physics Department, Aristotle University of Thessaloniki, 54124 Thessaloniki, Greece; gvourlia@auth.gr
* Correspondence: samkat@chem.auth.gr

Abstract: Nanotechnology presents promising opportunities for enhancing pest management strategies, particularly in protecting active ingredients to prolong their shelf life and effectiveness. Among different approaches, the combination of inorganic nanoparticles with active ingredients such as the main constituents of natural essential oils in one nanoarchitecture is challenging. In this study, hydrophobic calcium hydroxide nanoparticles coated with oleylamime [$Ca(OH)_2$@OAm NPs] were synthesized using microwave-assisted synthesis. These primary NPs were physicochemically characterized and subsequently utilized to prepare nanocapsules (NCs) either alone (Ca NCs) and/or in combination with geraniol at different ratios of $Ca(OH)_2$@OAm NPs and geraniol, i.e. 1:1 (CaGer1 NCs), 1:2 (CaGer2 NCs), and 1:3 (CaGer3 NCs), respectively. Among the formulations, the CaGer2 NCs demonstrated higher encapsulation efficiency (EE) and loading capacity (LC) of 95% and 20%, correspondingly. They exhibited a hydrodynamic size of 306 nm, a ζ-potential of -35 mV, and a monodisperse distribution. Release kinetics of geraniol from CaGer2 NCs indicated a pH-dependent slow release over 96 h at both 25 °C and 35 °C. In vitro antifungal assay against *B. cinerea* revealed a concentration-dependent activity, and the EC_{50} values for $Ca(OH)_2$@OAm NPs, Ca NCs, and CaGer2 NCs were estimated to be 654 µg/mL, 395 µg/mL, and 507 µg/mL, respectively. These results underscore the potential of Ca-based nanoformulations to control plant pathogens, suggesting that while Ca NCs showcase potent antifungal attributes, the different architectures/structures play a critical role in the antifungal effectiveness of the nanoformulations that have to be explored further.

Keywords: calcium hydroxide nanoparticles; inorganic nanoparticles; nano-delivery systems; antifungal efficacy; *Botrytis cinerea*; pH-responsive delivery

Citation: Tryfon, P.; Kamou, N.N.; Mourdikoudis, S.; Vourlias, G.; Menkissoglu-Spiroudi, U.; Dendrinou-Samara, C. Microwave-Mediated Synthesis and Characterization of $Ca(OH)_2$ Nanoparticles Destined for Geraniol Encapsulation. *Inorganics* **2023**, *11*, 470. https://doi.org/10.3390/inorganics11120470

Academic Editors: Roberto Nisticò, Torben R. Jensen, Luciano Carlos, Hicham Idriss and Eleonora Aneggi

Received: 23 October 2023
Revised: 28 November 2023
Accepted: 29 November 2023
Published: 2 December 2023

1. Introduction

The European Commission has set plant health very high on the political agenda since it is fundamental to our well-being and the environment. Plant pests can impact plant health causing serious economic and environmental effects. Therefore, plant protection from pests and diseases is of high priority in the European Union (EU). Since the 1940s, synthetic plant protection chemicals have substantially improved food production [1]. Synthetic fungicides, especially those targeting notorious pathogens like *Botrytis cinerea*

(*B. cinerea*), have been the frontline defense against fungal diseases [2]. However, the vast majority of these pesticides end up affecting non-target plants while culminating in significant environmental degradation and elevated health risks [1,3]. The resulting environmental and health implications highlight an urgent need for alternative, eco-friendly crop protection strategies.

Nanomaterials, with their versatile applications, offer novel solutions to this alarming situation [4]. Engineered inorganic nanoparticles (EINPs) provide substantial potential in plant protection. Their unique physicochemical characteristics facilitate effective fungal control and improve soil nutrient availability, while under specific nanoarchitectures, they enable the controlled release of antifungal agents [5,6]. EINPs have been observed to disrupt fungal cellular structures, inhibiting growth and ensuring the targeted delivery of antifungal agents [6]. However, with the progress of nanotechnology, advanced inorganic-based nanostructures have been developed with potential multifunctional properties that depend on their single counterparts. In that vein, and among different strategies for alternative plant protection agents, a promising pathway is the up-regulation of EINPs with natural active ingredients such as essential oils (EOs) or their constituents. Among them, geraniol, a monoterpene alcohol, is prominent. This highly hydrophobic natural product, derived from aromatic plants, is prevalent in various EOs. Due to its potent antimicrobial activity, geraniol has garnered research interest [7,8] and commercial products have already emerged in the market as plant protection products [9,10]. However, agents like geraniol are inherently unstable and volatile, which can hinder their efficacy [11]. An innovative approach within this domain is encapsulating EOs with EINPs. Encapsulation protects the active components of EOs, ensures their controlled release, and enhances delivery precision [11,12].

Thus, recent studies emphasize the synergistic potential of inorganic-based nanocapsules (NCs) and EOs in fighting plant pathogens. NCs formulated with *Zataria multiflora* and zinc oxide nanoparticles (ZnO NPs) demonstrated up to 66.33% increased efficacy against various *Fusarium* isolates and *A. solani* [13,14]. In studies with *B. cinerea*, pure geraniol and nanoemulsions containing geraniol showed EC_{50} values of 235 µg/mL and 105 µg/mL, respectively [15]. Furthermore, NCs integrating ZnO nanorods and geraniol effectively controlled *B. cinerea* without inducing phytotoxic effects in tomato and cucumber plants [9]. These results underline the significant role of NCs in enhancing essential oil efficiency against plant diseases.

Calcium (Ca) is an essential secondary nutrient that plays a crucial role in plant vitality [16]. Beyond its direct nutritional aspects, Ca is commonly applied in agriculture as a fertilizer and soil amendment [17,18]. This dual function of Ca-based compounds opens avenues for their potential fungicidal use while simultaneously enhancing cell wall fortification protection [19]. Notably, the European Food Safety Authority (EFSA) recently approved the use of calcium hydroxide [$Ca(OH)_2$] as a fungicide across various crops [20]. Calcium hydroxide nanoparticles [$Ca(OH)_2$ NPs] distinguish among the array of EINPs through their unique physical and chemical attributes, such as biocompatibility, non-toxicity, synthesis simplicity, and environmental compatibility [21]. The importance of $Ca(OH)_2$ NPs has been recognized in the past two decades, particularly in cultural heritage preservation [21] and dentistry [22]. Calcium-based nanoparticles (Ca-based NPs) are emerging as antibacterial candidates against a range of human pathogens, both Gram-negative (e.g., *Escherichia coli*, *Pseudomonas aeruginosa*) and Gram-positive (e.g., *Bacillus subtilis*, *Streptococcus aureus*) [23]. In the agricultural field, lime-based materials such as limestone ($CaCO_3$) and hydrated lime [$Ca(OH)_2$] are generally considered benign and beneficial when used to improve the soil pH, while each material exhibits diverse pH values and demonstrates a variety of functions. Also, Ca-based NPs have shown efficacy as nematicides against *Meloidogyne incognita* and *Meloidogyne javanica* as pH adjusters [24]. However, plant protection utilizing Ca-based nanoparticles (NPs) has received relatively less attention, despite their potential to be regarded as time-honored agents for phytoprotection.

Based on our previous efforts [9,25], in the present study, different nanoarchitectures were synthesized, characterized, and in vitro tested against *B. cinerea*. Initially, a microwave-assisted synthesis was applied to form relatively small hydrophobic nanoparticles of calcium hydroxide coated with oleylamine [$Ca(OH)_2$@OAm NPs]. These primary NPs were up-regulated to calcium-based nanocapsules (Ca-based NCs); (i) solely (Ca NCs) and (ii) in the presence of geraniol at varying ratios (1:1 for CaGer1, 1:2 for CaGer2, and 1:3 for CaGer3 NCs, respectively) in an attempt to optimize the most efficient formulation. The biodegradable and biocompatible surfactant, sodium dodecyl sulfate (SDS) was used as an emulsifier in all NCs. Comprehensive physicochemical analysis of both primary as-synthesized $Ca(OH)_2$@OAm NPs and the subsequent Ca-based NCs was undertaken using a range of techniques. Moreover, the influence of pH and kinetic analysis was explored for the case of CaGer2 NCs based on different models (first-order, Higuchi, and Korsmeyer–Peppas) at two different temperatures (25 °C and 35 °C) to assess the stability and release behavior of geraniol. An in vitro antifungal evaluation against *B. cinerea* was followed for the primary NPs and the secondary structures of NCs to test their efficacy against the well-known phytopathogen.

2. Results and Discussion

2.1. Physicochemical Characterization of $Ca(OH)_2$@OAm NPs

An X-ray diffractogram of the $Ca(OH)_2$@OAm NPs is presented in Figure 1, revealing a hexagonal $Ca(OH)_2$ in the portlandite phase (JCPDS pdf card #72-0156) [26]. Prominent peaks in the diffraction pattern are evident at angles (2θ) of 18.2°, 28.9°, and 34.4°, corresponding to (001), (100), and (011) reflections, respectively. These well-defined and pronounced diffraction peaks indicate a highly crystalline nature of the material. Utilizing the Scherrer formula based on the (011) plane, the crystalline size was determined to be 27 nm. This size is notably smaller than that observed for tannic acid-coated and PEGylated $Ca(OH)_2$@PEG NPs, which measured 50 nm and 40 nm, respectively [24,27]. The smaller crystalline size of the $Ca(OH)_2$@OAm NPs could be substantial in applications due to the increased surface area, enhanced diffusion, improved stability, and greater reactivity that it can provide. The crystallinity of the $Ca(OH)_2$@OAm NPs was established at 81.7%. Such distinct crystallinity suggests the potential suitability of the current NPs for applications that demand superior mechanical properties, particularly those requiring increased strength and density [28].

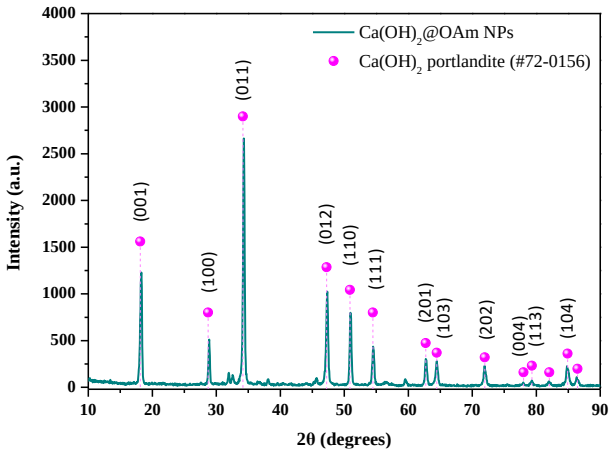

Figure 1. X-ray diffraction (XRD) of $Ca(OH)_2$@OAm NPs synthesized with the microwave-assisted process.

Functional groups present in the $Ca(OH)_2$@OAm NPs were evaluated with FT-IR spectroscopy, as depicted in Figure S1. The FT-IR spectrum exhibits prominent bands that correspond to diverse functional groups in the sample. A prominent and intense peak at 3642 cm^{-1} signifies the stretching mode of the –OH group, corroborating the presence of

$Ca(OH)_2$ [24,29]. The observed peaks at 2922 cm^{-1} and 2853 cm^{-1} can be assigned to the asymmetric and symmetric stretching vibrations of CH_2 groups, respectively, indicative of the characteristic OAm surfactant [9]. Additionally, the peak at 3347 cm^{-1} corresponds to the stretching vibration of N–H bonds, while the peaks at 1608 cm^{-1} and 1452 cm^{-1} are attributed to NH_2 bending and C–H bending vibrations, respectively [30,31]. The peak observed at 430 cm^{-1} corresponds to the characteristic Ca–O stretching vibration band, confirming the formation of $Ca(OH)_2$ particles [24,32].

The TEM analysis of $Ca(OH)_2$@OAm NPs helped to visualize their morphology. Figure 2 presents a TEM image of the NPs, showcasing particles with a hexagonal shape and an edge size in the range of a few hundred nanometers. Despite their thorough washing, the structures appear to be surrounded by an organic coating on their surface, which is associated with the use of OAm as a ligand. The observed structures exhibit a platelet-like morphology. The small thickness is indicated by the light contrast in the TEM images. OAm as a ligand favored this particle morphology by acting as a growth modifier. A partial tendency for agglomeration between the distinct nanoplates was noticed for the depicted $Ca(OH)_2$@OAm NPs.

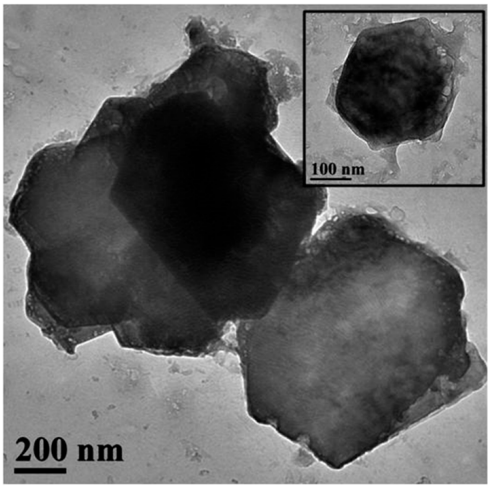

Figure 2. Transmission electron microscope (TEM) image of hexagonal $Ca(OH)_2$@OAm NPs at a scale of 200 nm (inset: scale at 100 nm).

A thermal stability study of $Ca(OH)_2$@OAm NPs was performed using TGA over the temperature range of 25 to 850 °C. An examination of the $Ca(OH)_2$@OAm NPs curve delineates three distinct stages of weight loss, as illustrated in Figure 3. The first weight loss step, accounting for approximately 8% *w*/*w*, occurs up to 120 °C and corresponds to the evaporation of physically adsorbed water molecules and/or loosely bound hydroxyl groups from the particle surface [33,34]. A subsequent 8% *w*/*w* decrement, materializing near 300 °C, results from the thermal decomposition of the OAm ligand [35]. OAm, commonly used as a surface-capping agent in metal oxide NP synthesis, decomposes upon heating, leading to the generation of volatile products such as ammonia, alkenes, and alkanes. This OAm detachment reflects the interplay of non-covalent interactions (hydrogen bonds and/or *van der Waals* forces) onto the particle surface, whereas the attrition at escalated temperatures signifies the disruption of covalent bonds [36]. The final weight loss step (15% *w*/*w*) takes place around 500 °C and is concurrent with the emergence of calcium oxide (CaO) within a 400–460 °C interval [32], notwithstanding the potential ongoing OAm ligand decomposition. Additionally, the DTG plot indicates a positive peak, validating the occurrence of the endothermic reaction in the conversion of $Ca(OH)_2$ into CaO, which is concomitant with the removal of water.

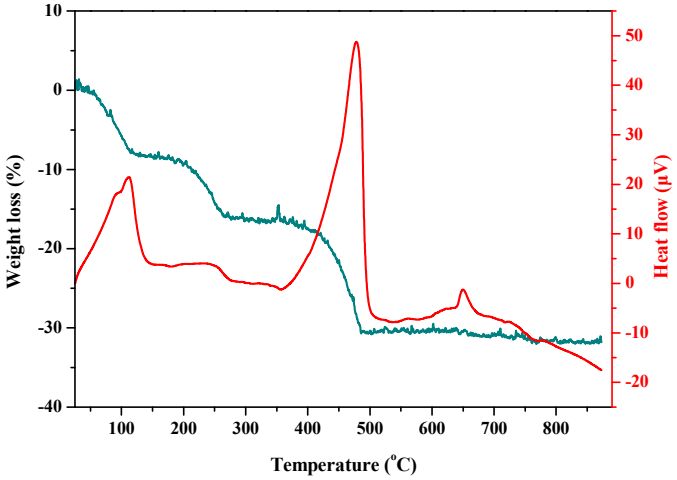

Figure 3. Thermogravimetric analysis (TGA) and derivative thermogravimetric (DTG) of the $Ca(OH)_2$@OAm NPs are presented with blue and red line, respectively.

UV-Vis spectroscopy was used to investigate the optical properties of $Ca(OH)_2$@OAm NPs. A solution containing dispersed $Ca(OH)_2$@OAm NPs in an ethanol/water (1:2) mixture was utilized to explore their absorption properties within the wavelength range of 210−600 nm. This choice of solvent offered high colloidal ability. The absorption spectrum (Figure S2A) of the NPs displayed two distinct absorbance bands observed at approximately 234 and 270 nm, corresponding to electronic transitions within the material. Additionally, a peak at 225 nm was observed, which is attributed to the presence of crystallized OAm. It is important to note that the cutoff wavelengths for water and ethyl alcohol are 190 and 210 nm, respectively. The absence of a shoulder in the absorption spectra indicates that the $Ca(OH)_2$@OAm NPs possess a direct band gap energy, signifying transitions from the valence band to the conduction band. Furthermore, the calculated band gap of the $Ca(OH)_2$@OAm NPs, determined from the Tauc plot (Figure S2B), was approximately 4 eV. This value is lower than the band gap of the naked $Ca(OH)_2$ NPs with a similar crystallite size (25 nm) at 5.20 eV, indicating a blue shift, in agreement with previous reports [29,32]. Generally, a larger band gap energy corresponds to higher electrical resistance and lower optical absorption, whereas a smaller band gap energy indicates an opposite trend.

Investigation into the physical properties of $Ca(OH)_2$@OAm NPs focused on determining the average particle size and ζ-potential value. The results revealed a mean particle size of 221 ± 0.4 nm (Figure S3A), indicating the size distribution of these NPs. Furthermore, ζ-potential assessments showed a value of +6.45 ± 0.85 mV (Figure S3B), suggesting a slight positive charge on the surface of particles. It is pertinent to highlight that agglomeration of NPs might transpire, owing to multiple factors such as weak inter-particle interactions, electrostatic attraction, and *van der Waals* forces, potentially culminating in particle clustering.

2.2. Physicochemical Characterization of Calcium-Based Nanocapsules

The emulsifier SDS was used in all NC formations at critical micelle concentration (CMC, 19.5 mM). SDS, which is an anionic surfactant commonly used in a variety of industrial and laboratory applications, plays a pivotal role in NC preparation by stabilizing emulsions, preventing particle aggregation, and controlling the release of encapsulated substances [37,38]. The evaluation of NC formulations for the smart delivery of bioactive agents in various bio-applications relies on parameters such as EE% and LC%. In the current study, the EE% and LC% of the three Ca-based NCs (CaGer1 NCs, CaGer2 NCs, and CaGer3 NCs) exhibited variations. EE% values were 43%, 95%, and 80% for CaGer1 NCs, CaGer2 NCs, and CaGer3 NCs, respectively. Conversely, the LC% values were 5%, 20%, and 24% for CaGer1 NCs, CaGer2 NCs, and CaGer3 NCs, correspondingly. The successful encapsulation and higher geraniol content compared with NCs combining ZnO@OAm

nanorods and geraniol (ZnOGer NCs) with the SDS stabilizer [9] may be attributed to the hydroxyl donors from $Ca(OH)_2$ that interact with the geraniol molecule, which contains a free –OH group [39]. This interaction allows for enhanced loading and encapsulation efficiency of geraniol in the CaGer NCs.

DLS measurements were conducted to assess the hydrodynamic size and ζ-potential of the NCs. The DLS analysis demonstrated that the hydrodynamic sizes of the NCs were 280 ± 2.3 nm (PDI = 0.328), 351 ± 1.1 nm (PDI = 0.064), and 306 ± 2.3 nm (PDI = 0.161) for Ca NCs (Figure S4A), CaGer1 NCs (Figure S4B), and CaGer2 NCs (Figure S4C), respectively. The hydrodynamic sizes are close, and size monodispersity is observed except for CaGer3 NCs, which displayed a polydisperse nature characterized by a multiple-size distribution by intensity, as shown by the presence of three distinct peaks and a relatively higher PDI rate of 0.423 (Figure S3D). This observation can be attributed to geraniol diffusion from the core of the NCs. The increase in the molecular weight and volume of geraniol necessitates the reorientation of polymeric chains, resulting in a less uniform particle size distribution in the CaGer3 NCs formulation. Regarding the ζ-potential, all formulations displayed negative values, with ζ-potential rates of −35.25 ± 0.57 mV for CaGer1 NCs, −35.40 ± 0.74 mV for CaGer2 NCs, and −41.3 ± 0.52 mV for CaGer3 NCs, respectively. The physicochemical characteristics of CaGer NCs are summarized in Table 1.

Table 1. Physicochemical characteristics of the calcium-based nanocapsules (Ca-based NCs).

Nano-Formulations	Mass Ratio NPs/Geraniol	Encapsulation Efficacy (%)	Loading Capacity (%)	DLS (d.nm)	PDI	ζ-Potential (mV)
CaGer1 NCs	1:1	43	5	351 ± 1.1	0.064	−35.2 ± 0.57
CaGer2 NCs	1:2	95	20	306 ± 2.3	0.161	−35.4 ± 0.74
CaGer3 NCs	1:3	80	24	382 ± 1.1	0.423	−41.3 ± 0.52

2.3. pH-Dependent Release Profiles and Kinetic Analysis of CaGer2 Nanocapsules

Plant growth is influenced by various environmental factors, including temperature and pH conditions, which play a crucial role in plant physiology and agricultural applications. Generally, pesticides can be degraded in soil, and the rate and type of chemical degradation are influenced by soil temperature, pH levels, moisture, and the binding of insecticides to the soil [40]. The pH of the surrounding environment can affect the release of entrapped ingredients [41] for several reasons: (i) the pH-dependent release behavior provides valuable insights into the potential of the NCs as pH-responsive delivery systems, (ii) changes in pH can alter the electrostatic interactions between the components of the NCs, leading to structural changes or disintegration of the capsules, and (iii) pH can affect the chemical properties of the environment surrounding the NCs. Additionally, temperature can modulate the release of geraniol from the NCs, with high temperatures generally resulting in a higher release rate compared with lower temperatures [9,15]. This can be attributed to the effects of temperature on the molecular mobility and diffusion properties of the encapsulated geraniol and the NC system. Higher temperatures increase the kinetic energy of the molecules, promoting faster diffusion and release of geraniol from the NCs. Temperature can also affect the solubility of geraniol and the interactions between geraniol and the NC matrix. Furthermore, it can impact the stability and integrity of the NCs, as higher temperatures may induce changes in the structure and properties of the NCs, leading to increased porosity or destabilization.

We investigated the effect of pH (values at 9.2, 7.2, and 5.2) on the release kinetics of geraniol from CaGer2 NCs at different temperatures of 25 °C and 35 °C due to their higher colloidal stability, lower hydrodynamic size, and EE% value than CaGer1 NCs and CaGer3 NCs. For the release mechanism of geraniol, the release data were fitted to various kinetic models, and the regression coefficients were analyzed (Tables S1 and S2). The geraniol release profile of CaGer2 NCs at 25 °C exhibited cumulative release percentages ($Q_{4h\%}$) of 7%, 16%, and 20% for pH values of 9.2, 7.2, and 5.2, respectively (Figure 4A). The first-order

model demonstrated a slow-release trend (Figure 4B) with an R^2 value of 0.965 at pH 9.2. Interestingly, the burst release rate at pH 7.2 in PBS media ($Q_{4h\%}$ = 36%) was lower compared with ZnOGer2 NCs [9] and native geraniol ($Q_{4h\%}$ = 55%) [15], resulting in an overall $Q_{96h\%}$ of 36% lower than that of ZnO-based NCs. The Higuchi model confirmed a diffusion mechanism release (Figure 4C), as evidenced by decreasing R^2 values (0.965, 0.949, and 0.914) and K_H values (6.43, 5.69, and 5.54) as pH decreased from 9.2 to 5.2. Moreover, the evaluation of the Korsmeyer–Peppas model revealed a normal Fickian diffusion mechanism for geraniol release from CaGer2 NCs in solutions with pH 7.2 and 5.2 (Figure 4D). However, a non-Fickian mechanism (anomalous diffusion) was observed at the highest pH (pH = 9.2), characterized by an exponent (*n*) greater than 0.45, which exhibited the best fit with the experimental data and system dimension [42].

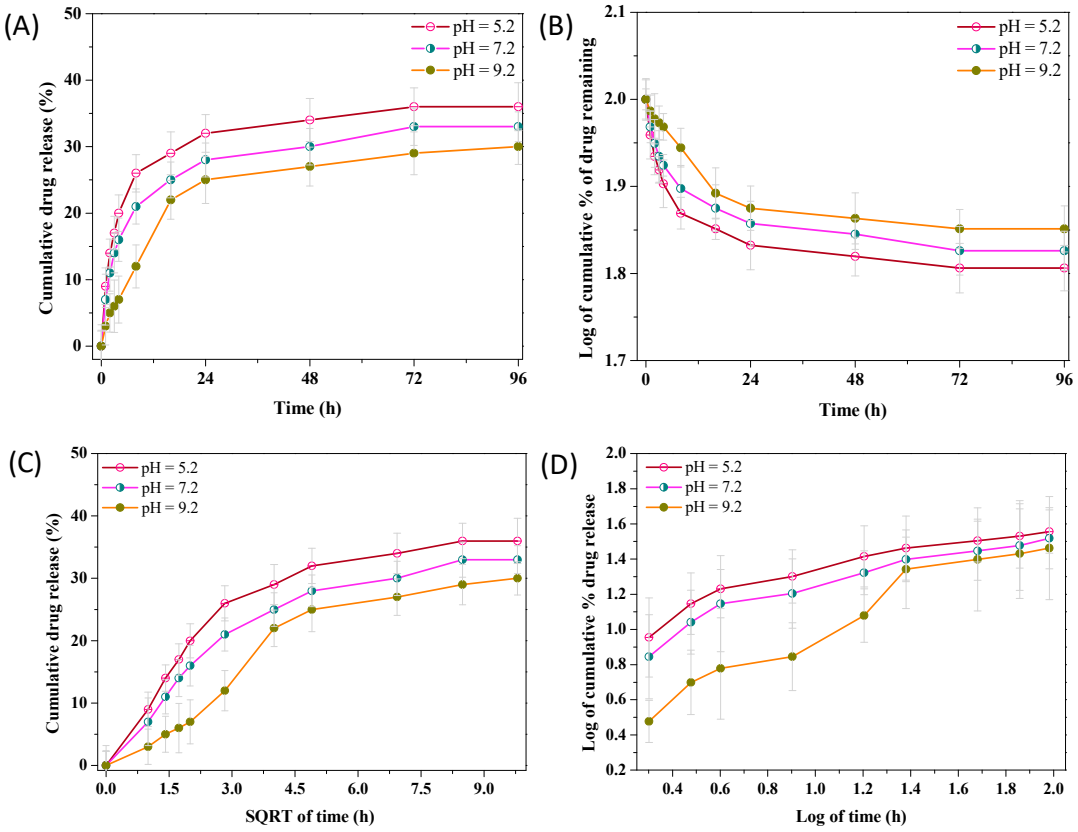

Figure 4. The pH-dependent release profiles of CaGer2 NCs were investigated under various pH conditions (pH = 9.2, 7.2, and 5.2) at a temperature of **25** ± 0.5 °C to simulate environmental conditions. The release profiles of geraniol were analyzed using four kinetic models: zero-order (**A**), first-order (**B**), Higuchi (**C**), and Korsmeyer–Peppas (**D**).

Both diffusion processes and macromolecule relaxation influenced the release process, with solvent diffusion and polymer relaxation transpiring at analogous rates. This triggered/delayed release phenomenon was particularly noticeable under alkaline conditions, resulting in consecutive release profiles over an extended period. Solvent diffusion proceeded at a markedly slower pace compared to micellar relaxation (evidenced by swelling and/or core erosion). The samples displayed an initial burst release followed by a slower continuous drug release over 96 h, indicating an immediate release trend [43]. Also, the pH values in the media affected the size distribution of CaGer2 NCs, as presented in Table S3, with 312 nm (PDI = 0.106) at pH 9.2 and 287 nm (PDI = 0.183) at pH 5.2.

The observed variations in release profiles can be attributed to the architectural differences among the nanosystems, as reported in previous studies where NCs with ZnO nanorods and geraniol [9] and geraniol-loaded nanoparticles prepared with the polymer Pluronic® F-127 [44] demonstrated sustained release over 24 h.

The kinetic profiles of geraniol release from CaGer2 NCs at a higher temperature (35 ± 0.5 °C) revealed cumulative release percentages ($Q_{4h\%}$) of 24%, 30%, and 22% at pH values of 9.2, 7.2, and 5.2, respectively (Figure 5A). A noticeable initial burst release of geraniol from the micelles was observed at pH 5.2 and a temperature of 35 °C. The release rate of geraniol was slightly slower ($Q_{4h\%}$ = 30%) at neutral pH compared with ZnOGer2 NCs [9]. The observed burst release of geraniol (at pH 5.2 and 35 °C) can lead to several potential impacts including faster drug delivery. Burst release can result in rapid delivery of the encapsulated drug/geraniol, which could be beneficial in certain applications where rapid drug action is required. Using the first-order model for NCs at pH 5.2 (Figure 5B) revealed a higher R^2 value (R^2 = 0.953), suggesting a more robust correlation among the variables and a superior data fit to the linear model than was observed at other pH levels (Table S2). Subsequent analysis of geraniol release over time utilized the Higuchi model (Figure 5C), where elevated K_H values signified a more rapid release rate (K_H = 7.24 at pH 5.2) compared with other conditions. Therefore, based on the obtained K_H values, it can be inferred that the release of geraniol from the NCs followed the Higuchi model for all samples. The Korsmeyer–Peppas model (Figure 5D) revealed a non-Fickian diffusion release of geraniol from CaGer2 NCs at pH 5.2 ($n > 0.45$), while a normal Fickian diffusion behavior was observed for the other two cases. Non-Fickian diffusion generally involves a combination of diffusion and other release mechanisms such as swelling, erosion, or polymer relaxation [45]. Hence, the primary mechanism of release from the micelles is considered to be drug diffusion. These measurements highlight the influence of pH on the stability and release behavior of geraniol, providing valuable insights for optimizing the formulation for effective plant protection.

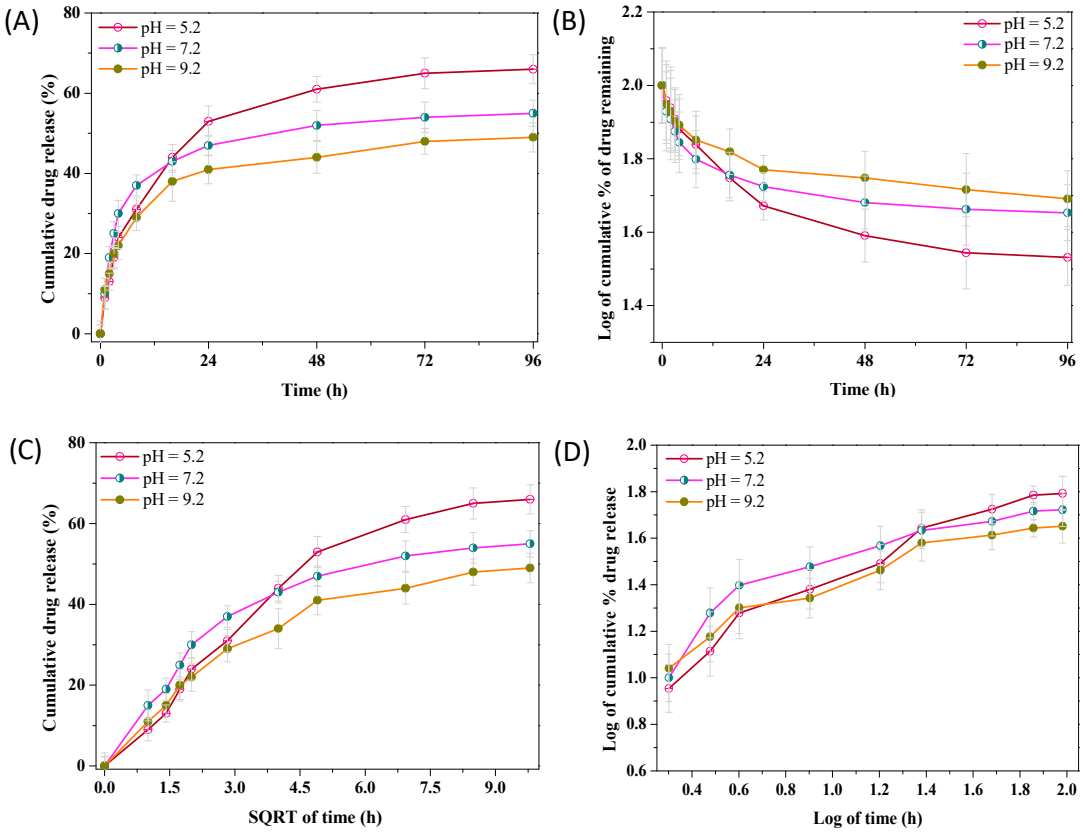

Figure 5. The pH-dependent release profiles of CaGer2 NCs were studied under various pH conditions (pH = 9.2, 7.2, and 5.2) at a temperature of **35** ± 0.5 °C to simulate environmental conditions. The release profiles of geraniol were processed using four kinetic models: zero-order (**A**), first-order (**B**), Higuchi (**C**), and Korsmeyer–Peppas (**D**).

After all, differentiations of the release profile of geraniol from pH and temperature may be considered as a limitation for further application. However, it is important to note that when acute treatment is needed, burst release can be potentially beneficial as rapid depletion of the drug occurs, while sustained release could be favorable in the case of early stages of affection and/or for preventive purposes.

2.4. In vitro Evaluation of Antifungal Activity of Ca-Based NPs and NCs

A preliminary estimation of the antifungal activity against *B. cinerea* of the Ca-based nanoformulations was undertaken. The efficacy of the primary $Ca(OH)_2$@OAm NPs and the Ca-based NCs: Ca NCs and CaGer2 NCs, were evaluated in vitro against *B. cinerea* by measuring their respective EC_{50} values. The determined EC_{50} values for $Ca(OH)_2$@OAm NPs, Ca NCs, and CaGer2 NCs against this pathogen were 654 μg/mL, 395 μg/mL, and 507 μg/mL, respectively, after 96 h (Table 2). The dose–response curves (Figure S5) and mycelium growth in Petri discs (Figure 6) for each case are presented. Interestingly, Ca NCs exhibited higher antifungal efficacy compared with CaGer2 NCs and $Ca(OH)_2$@OAm NPs. Nevertheless, lower EC_{50} values were found before by us in the case of pure geraniol and nanoemulsions containing geraniol against *B. cinerea* [15]. Moreover, NCs composed of ZnO and geraniol in molar ratios of 1:1 and 1:2 exhibited EC_{50} values of 176 μg/mL and 150 μg/mL *against B. cinerea*, respectively [9]. However, a straightforward correlation is not accurate due to the distinct metal base, indicating also that the derived nanostructures can exhibit properties not observed for any of the individual components.

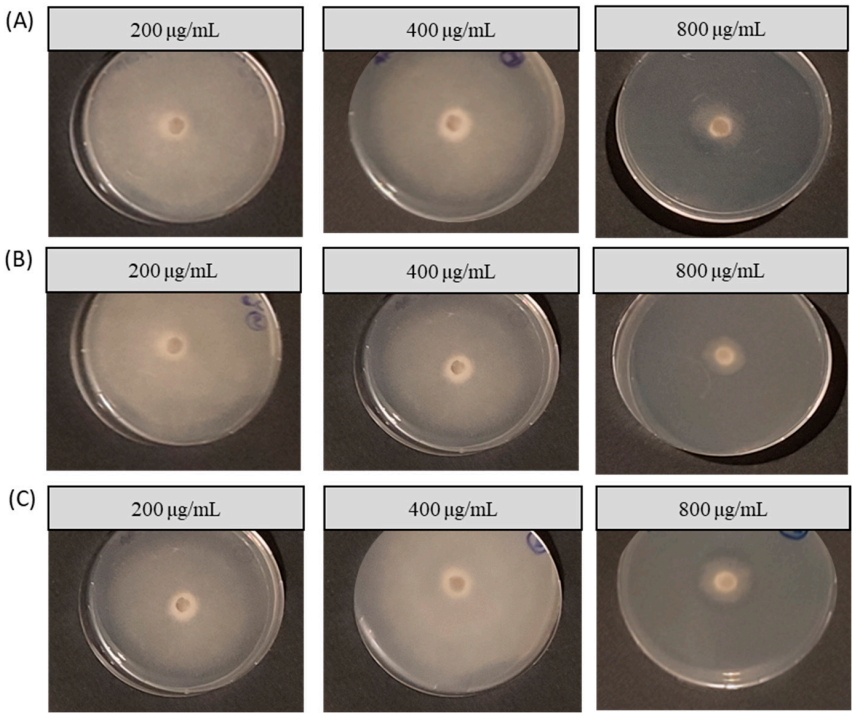

Figure 6. In vitro evaluation of the antifungal activity of $Ca(OH)_2$@OAm NPs (**A**), Ca NCs (**B**), and CaGer2 NCs (**C**) against *B. cinerea* was conducted on Petri plates containing PDA media 96 h after treatment.

Table 2. Half-maximal effective concentration (EC_{50} values) after the application of the Ca-based nanoformulations to *Botrytis cinerea*.

Treatments	EC_{50} Values (μg/mL) ± SDV
$Ca(OH)_2$@OAm NPs	654 ± 0.54
Ca NCs	395 ± 0.73
CaGer2 NCs	507 ± 0.75

3. Materials and Methods

3.1. Materials

Chemicals and Reagents. All chemicals and reagents were of analytical grade and were used without any further purification: calcium chloride (ACS, VWR Chemicals BDH®, Darmstadt, Germany, M = 110.9 g/mol, $CaCl_2$), oleylamine (Merck, Darmstadt, Germany, M = 267.493 g/mol, OAm), sodium hydroxide (Merck, M = 39.997 g/mol, NaOH), sodium dodecyl sulfate (Sigma-Aldrich, Darmstadt, Germany, ≥99%, M = 288.38 g/mol, SDS), chloroform (VWR Chemicals BDH®, ≥99.8%, $CHCl_3$), diethyl ether (Merck, ≥99%, M = 74.12 g/mol), geraniol (Sigma-Aldrich, 98%, M = 154.25 g/mol, trans-3,7-Dimethyl-2,6-octadien-1-ol), phosphate-buffered saline (Gibco by Life Technologies, Waltham, MA, USA, pH 7.2, 10X, PBS), and potato dextrose agar (BD Difco, Franklin Lakes, NJ, USA, PDA).

3.2. Synthesis of $Ca(OH)_2$@OAm NPs

A microwave-assisted (MW) route was used for the one-pot synthesis of $Ca(OH)_2$@OAm NPs: 10 mL of a 1.5 M NaOH aqueous solution was added dropwise to 0.8 g of anhydrous $CaCl_2$, which was then dissolved in 30 mL of OAm under vigorous stirring. This mixture was stirred continuously at 35 °C for 15 min before being transferred to a Teflon vessel. The reaction was conducted at 190 °C with a hold time of 30 min and a 15 min ramp time heating step in a MARS 6-240/50-CEM commercial microwave accelerated reaction system, operating at a maximum frequency of 2450 MHz and power of 1800 W. After the microwave treatment, the autoclave was cooled naturally to room temperature. The resulting mixture was centrifuged at 5000 rpm for 20 min and washed three times with chloroform ($CHCl_3$), to remove unnecessary impurities and precursors. The reaction yield was calculated to be 76% based on the initial amount of metal precursor used in the synthesis process and the amount of metal actually incorporated into the NPs.

3.3. Preparation of CaGer Nanocapsules

Calcium@geraniol nanocapsules (CaGer NCs) were synthesized following a previously established method [9]. The synthesis process involved several steps: first, 10 mg of hydrophobic $Ca(OH)_2$@OAm NPs were dissolved in 2 mL of diethyl ether and sonicated for 15 min. Subsequently, pure commercial geraniol was dissolved in 1 mL of diethyl ether and mixed with the NP solution. The resulting mixture was then added to a 30 mL solution of deionized water (diH_2O) containing sodium dodecyl sulfate (SDS) at a critical micelle concentration (CMC) of 19.5 mM. The emulsion was formed with sonication in a closed vial under controlled conditions (<30 °C). After five hours, the vial was opened, and the diethyl ether was slowly evaporated to isolate the respective formulations of NCs: (i) CaGer1 NCs (NPs: geraniol mass ratio of 1:1), (ii) CaGer2 NCs (NPs: geraniol mass ratio of 1:2), and (iii) CaGer3 NCs (NPs: geraniol mass ratio of 1:3). A similar procedure was used for the preparation of calcium hydroxide nanocapsules (Ca NCs), except that this was carried out without adding geraniol. In all procedures, the CMC was maintained at a stable value.

3.4. Characterization Techniques

The crystalline size and structure of $Ca(OH)_2$@OAm NPs were determined using X-ray diffraction (XRD) analysis. XRD pattern was obtained using a two-cycle Rigaku Ultima+ X-ray diffractometer (Rigaku Corporation, Shibuya-Ku, Tokyo, Japan) with a Cu-Kα radiation source (1.541 Å) operating at 40 kV/30 mA. Estimation of the crystallite size was conducted using the Scherrer formula [46]. Furthermore, the crystallinity of the NPs was calculated following the method outlined by Khan et al. (2019) [47]:

$$Crystallinity\ (\%) = \frac{Area\ of\ crystalline\ peaks}{Area\ of\ all\ peaks} \quad (1)$$

Fourier-transform infrared (FT-IR) spectrum of the NPs was performed with a Nicolet iS20 FT-IR spectrometer (Thermo Fisher Scientific, Waltham, MA, USA), featuring a monolithic diamond attenuated total reflection (ATR) crystal, in the wavenumber range of 4000–450 cm^{-1}. TEM imaging was employed to study the morphology of the NPs using a JEOL JEM 1200-EX (Tokyo, Japan) microscope operating at an acceleration voltage of 120 kV. Samples were prepared by placing a drop of diluted NP suspension on a carbon-coated copper grid and air-drying at room temperature. Thermal studies were conducted using a SETA-RAM SetSys-1200 (KEP Technologies, Caluire, France) instrument. Differential thermogravimetric (DTG) and thermogravimetric analysis (TGA) measurements were performed under a nitrogen (N_2) atmosphere with a heating rate of 10 °C/min. Optical property evaluation of the NPs was conducted with a UV-Vis spectrophotometer (V-750, Jasco, Tokyo, Japan), and the band gap energy was calculated based on Tauc's formula $\alpha h\nu = A(h\nu - E_g)^2$ [48]. Assessments of hydrodynamic size (nm), polydispersity index (PDI), and ζ-potential (mV) for the freshly synthesized NCs and NPs were carried out using dynamic light scattering (DLS) analysis at 25 °C, utilizing a Zetasizer (Nano ZS Malvern apparatus VASCO Flex™ Particle Size Analyzer NanoQ V2.5.4.0, Malvern, UK).

3.5. Encapsulation Efficiency and Loading Capacity

Encapsulation efficiency (EE, %) and loading capacity (LC, %) for the nanosystems were calculated to evaluate the compatibility of geraniol with, and the effectiveness of its integration into, CaGer NCs. Evaluation of the EE and LC of geraniol was conducted based on the methodology delineated in prior research [9]. These essential parameters indicate the quantity of geraniol effectively incorporated into the NCs and the overall efficiency of the encapsulation procedure.

3.6. pH-Dependent Release Profiles of Geraniol

The in vitro release profile of geraniol from CaGer NCs was assessed using a dialysis membrane (Pur-A-Lyzer Midi 1000) at two different temperatures: (i) 25 ± 0.5 °C and (ii) 35 ± 0.5 °C. Briefly, 1 mL of the nanoformulation was placed inside a dialysis bag, which was then immersed in 40 mL of PBS solution with varying pH values (9.2, 7.2, and 5.2). The entire system was kept at a constant temperature and stirring rate for 96 h. At predetermined time intervals, 2 mL of the release media was collected and replaced with an equal volume of fresh PBS. The concentration of released geraniol was measured using a UV-Vis spectrophotometer. The obtained data were subjected to mathematical modeling using various models, including zero-order, first-order, Higuchi, and Korsmeyer-Peppas, to determine the transport mechanism, release type, and kinetics of geraniol release [49–51]. Each experiment was performed in triplicate (n = 3) to ensure the reliability and reproducibility of the results.

3.7. Fungal Strain and Growth Conditions

The *Botrytis cinerea* (*B. cinerea*) strain B05 used in this study was obtained from the culture collection of the Plant Pathology Laboratory at the Aristotle University of Thessaloniki. The strain was maintained on potato dextrose agar (PDA) plates at 25 °C in a controlled environment.

3.8. Antifungal Activity Assay

The antifungal activity of $Ca(OH)_2$@OAm NPs, Ca NCs, and CaGer2 NCs was evaluated by mixing the nanoformulations with PDA media and measuring the impact on the growth of *B. cinerea*. To prevent the degradation of the nanoformulations, the media were maintained at approximately 40 °C during the process. Various concentrations of $Ca(OH)_2$@OAm NPs (100, 200, 400, 600, 800, and 1000 μg/mL) and NCs (20, 80, 200, 400, 600, 800, and 1000 μg/mL) were tested. The inhibitory effect of these concentrations on mycelial growth was then assessed. The half-maximal effective concentration

(EC_{50}) value, which is the concentration required to inhibit 50% of mycelial growth, was determined [52,53].

3.9. Statistical Evaluation

The EC_{50} values in the in vitro bioassays were determined according to a non-linear dose-response curve and ten replicates per sample concentration using Origin Pro 8 (Data Analysis and Graphing Software 8.0). Data in kinetic release models were calculated based on the mean of three independent measurements with standard deviations.

4. Conclusions

The development of innovative nanoformulations for the enhanced and targeted control of phytopathogens is challenging. Advanced, second-generation structures amplify advantages primarily due to their unique material properties. In the pursuit of sustainable and eco-friendly solutions for crop protection, $Ca(OH)_2$@OAm NPs were synthesized, which emerged as potent platforms for the encapsulation of geraniol. Remarkably, the $Ca(OH)_2$@OAm NPs were produced with high yields and crystallinity using a one-step and reproducible, microwave-assisted synthesis. The primary NPs were advanced to secondary nanostructures, Ca NPs, CaGer1 NCs, CaGer2 NCs, and CaGer3 NCs, using the emulsifier SDS. Among these, CaGer2 NCs exhibited efficient encapsulation and loading of geraniol, boasting an encapsulation efficiency (EE) of 95% and a loading capacity (LC) of 20%. The release profile evaluation of CaGer2 NCs revealed that variations in pH and temperature influence the release rate of geraniol from the NCs. Antifungal assays against *B. cinerea* showed that Ca NCs demonstrated the highest inhibition in the fungal growth, with an EC_{50} value of 395 µg/mL. Encapsulated $Ca(OH)_2$@OAm NPs demonstrated enhanced efficacy against *B. cinerea* compared with individual NPs. Nonetheless, the newly developed CaGer2 NCs did not exhibit synergistic effects. Further studies are required to test these nanoformulations on a broader spectrum of microorganisms and their potential impact on non-target organisms in order to be deployed for in planta applications.

Supplementary Materials: The following supporting information can be downloaded at: https://www.mdpi.com/article/10.3390/inorganics11120470/s1, Figure S1: FT-IR spectrum of $Ca(OH)_2$@OAm NPs; Figure S2: Absorption spectra as a function of wavelength (210–600 nm) (A) and Tauc plots of $(\alpha h\nu)^2$ vs. $h\nu$ with linear relationship (B) for $Ca(OH)_2$@OAm NPs in ethanol/water solution; Figure S3: Hydrodynamic diameter distribution measured with DLS and ζ-potential for $Ca(OH)_2$@OAm NPs suspension; Figure S4: Hydrodynamic diameter distribution was measured with DLS for the supernatant of CaGer1 NCs (A), CaGer2 NCs (B), and CaGer3 NCs (C) at 25 °C; Table S1: The values (R^2, K_H, n) for the pH-dependent release profiles of CaGer2 NCs are determined using mathematical models: zero-order, first-order, Higuchi, and Korsmeyer-Peppas. The measurements were performed under 25 °C and different pH values (9.2, 7.2, and 5.2) in triplicate; Table S2: The values (R^2, K_H, n) for the pH-dependent release profiles of CaGer2 NCs are derived using mathematical models: zero-order, first-order, Higuchi, and Korsmeyer–Peppas. The measurements were performed under 35 °C and different pH values (9.2, 7.2, and 5.2) in triplicate; Table S3: Dynamic light scattering analysis and ζ-potential values of CaGer2 NCs at pH 5.2 and 9.2; Figure S5: Dose-response growth inhibition curves of *B. cinerea* in response to varying concentrations of $Ca(OH)_2$@OAm nanoparticles (A), Ca nanocapsules (B), and CaGer2 nanocapsules (C). Each data point represents the mean of ten replicates per nanoformulation concentration (2 experiments, 5 replications) 96 h after application.

Author Contributions: Conceptualization, C.D.-S.; methodology, P.T. and N.N.K.; software, P.T., S.M. and G.V.; validation, C.D.-S. and U.M.-S.; formal analysis, P.T.; investigation, P.T., S.M., N.N.K. and G.V.; resources, C.D.-S. and U.M.-S.; data curation, P.T.; writing—original draft preparation, P.T.; writing—review and editing, C.D.-S. and U.M.-S.; visualization, P.T. and S.M.; supervision, C.D.-S. and U.M.-S.; project administration, C.D.-S. and U.M.-S. All authors have read and agreed to the published version of the manuscript.

Funding: Tryfon Panagiota acknowledges the financial support from Greece and the European Union (European Social Fund-ESF) through the Operational Programme "Human Resources Development, Education and Lifelong Learning" in the context of the Act "Enhancing Human Resources Research Potential by undertaking a Doctoral Research" Sub-action 2: IKY Scholarship Programme for PhD candidates in Greek Universities (MIS-5113934).

Data Availability Statement: The data presented in this study are available in this article.

Conflicts of Interest: The authors declare no conflict of interest.

References

1. Bernardes, M.F.F.; Pazin, M.; Pereira, L.C.; Dorta, D.J. Impact of Pesticides on Environmental and Human Health. In *Toxicology Studies-Cells, Drugs, and Environment*; IntechOpen: London, UK, 2015; pp. 195–233.
2. Kim, J.-O.; Shin, J.-H.; Gumilang, A.; Chung, K.; Kim, K.S. Effectiveness of different classes of fungicides on *Botrytis cinerea* causing gray mold on fruit and vegetables. *Plant Pathol. J.* **2016**, *32*, 570–574. [CrossRef] [PubMed]
3. Hernández, A.F.; Gil, F.; Lacasaña, M.; Rodríguez-Barranco, M.; Tsatsakis, A.M.; Requena, M.; Alarcón, R. Pesticide exposure and genetic variation in xenobiotic-metabolizing enzymes interact to induce biochemical liver damage. *Food Chem. Toxicol.* **2013**, *61*, 144–151. [CrossRef] [PubMed]
4. Singh, J.; Yadav, A.N. Natural products as fungicide and their role in crop protection. In *Natural Bioactive Products in Sustainable Agriculture*; Springer: Singapore, 2020; Chapter 9; pp. 131–219.
5. Xu, J.-L.; Luo, Y.-X.; Yuan, S.-H.; Li, L.-W.; Liu, N.-N. Antifungal nanomaterials: Current progress and future directions. *Innov. Digit. Health Diagn. Biomark.* **2021**, *1*, 3–7. [CrossRef]
6. Huang, T.; Li, X.; Maier, M.; O'Brien-Simpson, N.M.; Heath, D.E.; O'Connor, A.J. Using inorganic nanoparticles to fight fungal infections in the antimicrobial resistant era. *Acta Biomater.* **2023**, *158*, 56–79. [CrossRef] [PubMed]
7. Chen, W.; Viljoen, A.M. Geraniol-A review of a commercially important fragrance material. *S. Afr. J. Bot.* **2010**, *76*, 643–651. [CrossRef]
8. Lira, M.H.P.; de Andrade Júnior, F.P.; Moraes, G.F.Q.; Macena, G.S.; Pereira, F.O.; Lima, I.O. Antimicrobial activity of geraniol: An integrative review. *J. Essent. Oil Res.* **2020**, *32*, 187–197. [CrossRef]
9. Tryfon, P.; Kamou, N.N.; Pavlou, A.; Mourdikoudis, S.; Menkissoglu-Spiroudi, U.; Dendrinou-Samara, C. Nanocapsules of ZnO nanorods and geraniol as a novel mean for the effective control of *Botrytis cinerea* in tomato and cucumber plants. *Plants* **2023**, *12*, 1074. [CrossRef]
10. Available online: https://food.ec.europa.eu/plants/pesticides/eu-pesticides-database_en (accessed on 5 September 2023).
11. Chaudhari, A.K.; Singh, V.K.; Das, S.; Dubey, N.K. Nanoencapsulation of essential oils and their bioactive constituents: A novel strategy to control mycotoxin contamination in the food system. *Food Chem. Toxicol.* **2021**, *149*, 112019. [CrossRef]
12. Pavoni, L.; Perinelli, D.R.; Bonacucina, G.; Cespi, M.; Palmieri, G.P. An overview of micro- and nanoemulsions as vehicles for essential oils: Formulation, preparation and stability. *Nanomaterials* **2020**, *10*, 135. [CrossRef]
13. Enayati, S.; Davari, M.; Habibi-Yangjeh, A.; Ebadollahi, A.; Feizpoor, S. Enhancement of the antifungal properties of Zataria multiflora essential oil through nanoencapsulation with ZnO nanomaterial. *Res. Sq.* **2021**, *42*, 503–513. [CrossRef]
14. Akhtari, A.; Davari, M.; Habibi-Yangjeh, A.; Ebadollahi, A.; Feizpour, S. Antifungal activities of pure and ZnO-encapsulated essential oil of Zataria multiflora on *Alternaria solani* as the pathogenic agent of tomato early blight disease. *Front. Plant Sci.* **2022**, *13*, 932475. [CrossRef] [PubMed]
15. Kamou, N.N.; Kalogiouri, N.P.; Tryfon, P.; Papadopoulou, A.; Karamanoli, K.; Dendrinou-Samara, C.; Menkissoglu-Spiroudi, U. Impact of geraniol and geraniol nanoemulsions on *Botrytis cinerea* and effect of geraniol on cucumber plants' metabolic profile analyzed by LC-QTOF-MS. *Plants* **2022**, *11*, 2513. [CrossRef] [PubMed]
16. White, P.J.; Broadley, M.R. Calcium in plants. *Ann. Bot.* **2003**, *92*, 487–511. [CrossRef] [PubMed]
17. McLaughlin, S.; Wimmer, R. Calcium physiology and terrestrial ecosystem processes. *New Phytol.* **1999**, *142*, 373–417. [CrossRef]
18. Parra-Terraza, S.; Villarreal-Romero, M.; Sánchez-Peña, P.; Corrales-Madrid, J.L.; Hernández-Verdugo, S. Effect of calcium and osmotic potential of the nutrient solution on the blossom end rot, mineral composition and yield of tomato. *Interscience* **2008**, *33*, 449–456.
19. Zhang, L.; Du, L.; Poovaiah, W.B. Calcium signaling and biotic defense responses in plants. *Plant Signal Behav.* **2014**, *9*, e973818. [CrossRef] [PubMed]
20. European Food Safety Authority (EFSA). *Outcome of the Consultation with Member States and EFSA on the Basic Substance Application for Approval of Calcium Hydroxide for the Extension of Use in Plant Protection as a Fungicide in Grapevine and Peach, and as Insecticide in Grapevine, Plum, Peach, Apricot, Apple, Pear, Almond and Strawberry*; EFSA Publications: Parma, Italy, 2020.
21. Zhu, J.; Zhang, P.; Ding, J.; Dong, Y.; Cao, Y.; Dong, W.; Zhao, X.; Li, X.; Camaiti, M. Nano $Ca(OH)_2$: A review on synthesis, properties and applications. *J. Cult. Herit.* **2021**, *50*, 25–42. [CrossRef]
22. Nishanthi, R.; Ravindran, V. Role of calcium hydroxide in dentistry: A review. *Int. J. Pharm. Res.* **2020**, *12*, 2822–2827.
23. Harish; Kumari, S.; Parihar, J.; Akash; Kumari, J.; Kumar, L.; Debnath, M.; Kumar, V.; Mishra, R.K.; Gwag, J.S.; et al. Synthesis, characterization, and antibacterial activity of calcium hydroxide nanoparticles against gram-positive and gram-negative bacteria. *ChemistrySelect* **2022**, *7*, e202203094. [CrossRef]

24. Tryfon, P.; Antonoglou, O.; Vourlias, G.; Mourdikoudis, S.; Menkissoglu-Spiroudi, U.; Dendrinou-Samara, C. Tailoring Ca-based nanoparticles by polyol process for use as nematicidals and pH adjusters in Agriculture. *ACS Appl. Nano Mater.* **2019**, *2*, 3870–3881. [CrossRef]
25. Gawande, M.B.; Shelke, S.N.; Zboril, R.; Varma, R.S. Microwave-Assisted Chemistry: Synthetic Applications for Rapid Assembly of Nanomaterials and Organics. *Acc. Chem. Res.* **2014**, *47*, 1338–1348. [CrossRef]
26. Musamali, R.W.; Isa, Y.M. Production of clean hydrogen from methane decomposition over molten NiO-LiOH catalyst systems supported on CaO: Synergistic effect of molten LiOH on catalyst activity. *Asia Pac. J. Chem. Eng.* **2021**, *16*, e2655. [CrossRef]
27. Chen, P.; Wang, Y.; He, S.; Wang, P.; Xu, Y.; Zhang, L. Green synthesis of spherical calcium hydroxide nanoparticles in the presence of tannic acid. *Adv. Mater. Sci. Eng.* **2020**, *2020*, 9501897. [CrossRef]
28. Fuzhi, S.; Wang, Q.; Wang, Y. The effects of crystallinity on the mechanical properties and the limiting PV (pressure × velocity) value of PTFE. *Tribol. Int.* **2016**, *93*, 1–10.
29. Kumar, P.; Kumari, J.; Kumar, L.; Salim, A.; Singhal, R.; Mukhopadhyay, A.K.; Joshi, R.P. Influence of chemical synthesis process on the properties of calcium hydroxide nanoparticles. *Mater. Today Proc.* **2022**, *60*, 153–159.
30. Mourdikoudis, S.; Liz-Marzán, L.M. Oleylamine in nanoparticle synthesis. *Chem. Mater.* **2013**, *25*, 1465–1476. [CrossRef]
31. Guo, H.; Chen, Y.; Cortie, M.B.; Liu, X.; Xie, Q.; Wang, X.; Peng, D.L. Shape-selective formation of monodisperse copper nanospheres and nanocubes via disproportionation reaction route and their optical properties. *J. Phys. Chem. C* **2014**, *118*, 9801–9808. [CrossRef]
32. Kumar, P.; Malhotra, B.; Phalswal, P.; Khanna, P.K.; Salim, A.; Singhal, R.; Mukhopadhyay, A.K. Effect of reaction rate on the properties of chemically synthesized calcium hydroxide nanoparticles. *Mater. Today Proc.* **2020**, *28*, 2305–2310.
33. Khachani, M.; El Hamidi, A.; Halim, M.; Arsalane, S. Non-isothermal kinetic and thermodynamic studies of the dehydroxylation process of synthetic calcium hydroxide $Ca(OH)_2$. *J. Mater. Environ. Sci.* **2014**, *5*, 615–624.
34. Samanta, A.; Podder, S.; Ghosh, C.K.; Bhattacharya, M.; Ghosh, J.; Mallik, A.K.; Dey, A.; Mukhopadhyay, A.K. ROS mediated high anti-bacterial efficacy of strain tolerant layered phase pure nano-calcium hydroxide. *J. Mech. Behav. Biomed. Mater.* **2017**, *72*, 110–128. [CrossRef]
35. Lan, F.; Bai, J.; Wang, H. The preparation of oleylamine modified micro-size sphere silver particles and its application in crystalline silicon solar cells. *RSC Adv.* **2018**, *8*, 16866. [CrossRef] [PubMed]
36. Lenin, R.; Joy, P.A. Role of primary and secondary surfactant layers on the thermal conductivity of lauric acid coated magnetite nanofluids. *J. Phys. Chem. C* **2016**, *120*, 11640–11651. [CrossRef]
37. Vamvakidis, K.; Mourdikoudis, S.; Makridis, A.; Paulidou, E.; Angelakeris, M.; Dendrinou-Samara, C. Magnetic hyperthermia efficiency and MRI contrast sensitivity of colloidal soft/hard ferrite nanoclusters. *J. Colloid Interf. Sci.* **2018**, *511*, 101–109. [CrossRef] [PubMed]
38. Antonoglou, A.; Giannousi, K.; Mourdikoudis, S.; Dendrinou-Samara, C. Magnetic nanoemulsions as candidates for alzheimer's disease dual imaging theranostics. *Nanotechnology* **2020**, *31*, 465702. [CrossRef]
39. Rajabi, H.; Mosleh, M.H.; Mandal, P.; Lea-Langton, A.; Sedighi, M. Emissions of volatile organic compounds from crude oil processing—Global emission inventory and environmental release. *Sci. Total Environ.* **2020**, *727*, 138654. [CrossRef]
40. Singh, D.K. Pesticides and environment. *Pestic. Chem. Toxicol.* **2012**, *1*, 114–122.
41. Zarepour, A.; Zarrabi, A.; Larsen, K.L. Fabricating β-cyclodextrin based pH-responsive nanotheranostics as a programmable polymeric nanocapsule for simultaneous diagnosis and therapy. *Int. J. Nanomed.* **2019**, *14*, 7017–7038. [CrossRef]
42. Ahmed, L.; Atif, R.; Salah Eldeen, T.; Yahya, I.; Omara, A.; Eltayeb, M. Study the using of nanoparticles as drug delivery system based on mathematical models for controlled release. *IJLTEMAS* **2019**, *8*, 52–56.
43. Wu, J.; Zhang, Z.; Gu, J.; Zhou, W.; Liang, X.; Zhou, G.; Han, C.C.; Xu, S.; Liu, Y. Mechanism of a long-term controlled drug release system based on simple blended electrospun fibers. *J. Control. Release* **2020**, *320*, 337–346. [CrossRef]
44. Yegin, Y.; Perez-Lewis, K.; Zhang, M.; Akbulut, M.; Taylor, T.M. Development and characterization of geraniol-loaded polymeric nanoparticles with antimicrobial activity against foodborne bacterial pathogens. *J. Food Eng.* **2016**, *170*, 64–71. [CrossRef]
45. Biondo, F.; Baldassarre, F.; Vergaro, V.; Ciccarella, G. Controlled Biocide Release from Smart Delivery Systems: Materials Engineering to Tune Release Rate, Biointeractions, and Responsiveness. In *Nanotechnology-Based Sustainable Alternatives for the Management of Plant Diseases*; Balestra, G.M., Fortunati, E., Eds.; Elsevier: Amsterdam, The Netherlands, 2022.
46. Cullity, B.D. *Elements of X-ray Diffraction*, 2nd ed.; Addison-Wesley Publishing Co., Ltd.: Reading, MA, USA, 1978.
47. Khan, A.; Toufiq, A.M.; Tariq, F.; Khan, Y.; Hussain, R.; Akhtar, N.; Rahman, S. Influence of Fe doping on the structural, optical, and thermal properties of α-MnO_2 Nanowires. *Mat. Res. Express* **2019**, *6*, 065043. [CrossRef]
48. Davis, E.A.; Mott, N.F. Conduction in non-crystalline systems V. Conductivity, optical absorption and photoconductivity in amorphous semiconductors. *Philos. Mag. A* **1970**, *22*, 903–922. [CrossRef]
49. Dash, V. Release kinetic studies of aspirin microcapsules from ethyl cellulose, cellulose acetate phthalate and their mixtures by emulsion solvent evaporation method. *Sci. Pharm.* **2010**, *78*, 93–101. [CrossRef] [PubMed]
50. Lokhandwala, H.; Deshpande, A.; Deshpande, S. Kinetic modeling and dissolution profiles comparison: An overview. *Int. J. Pharm. Bio. Sci.* **2013**, *4*, 728–773.
51. Ramteke, K.H.; Dighe, P.A.; Kharat, A.R.; Patil, S.V. Mathematical models of drug dissolution: A review. *Sch. Acad. J. Pharm.* **2014**, *3*, 388396.

52. Banik, S.; Pérez-de-Luque, A. In vitro effects of copper nanoparticles on plant pathogens, beneficial microbes, and crop plants. *Span. J. Agricult. Res.* **2017**, *15*, e1005. [CrossRef]
53. Tryfon, P.; Kamou, N.N.; Mourdikoudis, S.; Karamanoli, K.; Menkissoglu-Spiroudi, U.; Dendrinou-Samara, C. CuZn and ZnO Nanoflowers as nano-fungicides against *Botrytis cinerea* and *Sclerotinia sclerotiorum*: Phytoprotection, translocation, and impact after foliar application. *Materials* **2021**, *14*, 7600. [CrossRef]